IEEE Access
Multidisciplinary | Rapid Review | Open Access Journal

IEEE POWER & ENERGY SOCIETY SECTION

Received 31 July 2024, accepted 20 August 2024, date of publication 29 August 2024, date of current version 6 September 2024.

Digital Object Identifier 10.1109/ACCESS.2024.3450491

RESEARCH ARTICLE

Computational Features of Electric Machine Hybrid FEA-dq Dynamic Models

CHRISTIAN KUKURA, JUDITH APSLEY, (Senior Member, IEEE), AND SINIŠA DJUROVIĆ, (Member, IEEE)

Department of Electrical and Electronic Engineering, The University of Manchester, M13 9PL Manchester, U.K.

Corresponding author: Christian Kukura (author@boulder.nist.gov)

The work of Christian Kukura was supported by UKRI/EPSRC for funding Ph.D. Scholarship through a DTP Scheme at Department of Electrical and Electronic at University of Manchester.

ABSTRACT As the world focuses more on renewable generation, Permanent Magnet Synchronous Machines (PMSMs) are seeing greater use in wind turbines and electric vehicle applications. To address the computational demands of full fidelity machine models using Finite Element Analysis (FEA) or the expense of constructing an experimental test rig for practical performance analysis, adopting a dynamic hybrid electromagnetic FEA-dq model offers an accurate and computationally efficient means of analysing machine operation. This work aims to demonstrate what construction variables are essential to consider when building these models and how they influence the electromagnetic signals of the machine under both steady state and transient modes of operation. A conventional PMSM control strategy is employed in this work, and all sections focus exclusively on balanced PMSM operation under healthy conditions.

INDEX TERMS Finite element analysis, hybrid FEA-dq model, lookup table, PMSM.

I. INTRODUCTION

Over the last three decades, advances in technology have facilitated the application of energy-efficient high performance drives, enabling electric machines (EM) to be increasingly employed in the automotive and renewable generation industries as part of the global push for decarbonisation [1], [2], [3], [4]. This trend is anticipated to further increase, placing greater demands for improved performance electrical machinery.

Modelling plays a crucial role in the design, analysis and performance optimisation of electrical machines, where increased fidelity dynamic models with low computational expense are of growing interest [5]. Hybrid d-q models based on pre-calculated finite element analysis (FEA) electromagnetic model data have been increasingly employed in simulation studies and electric circuit analysis methods, ranging from analysis of the dynamic performance of Induction Machines (IMs) and Permanent Magnet Synchronous Machines (PMSMs) to simulating winding and demagnetisation faults [4], [6], [7], [8], [9]. Compared to the dynamic FEA-only electro-magnetic models, the hybrid models offer a significantly faster computational processing time. By incorporating the FEA pre-calculated electromagnetic characteristics in the form of multi-dimensional lookup tables (LUTs) that define the relationship between the d-q axes currents and flux linkages as a function of rotor position, nonlinear electromagnetic effects such as magnetic saturation and harmonic effects can be represented. A significant level of accuracy can be achieved, as shown in [10] where the average percentage error between measured and simulated torque was 1.74%. The resulting hybrid model allows low computational-intensity, non-linear, dynamic analysis of machine behaviour under a diverse range of operating conditions. Hybrid modelling has been utilised to accurately predict the electromagnetic characteristics in PMSMs employed in drive cycle applications [11], [12], [13]. Hybrid modelling was also implemented in [19] for rated operating condition and load change with harmonic analysis of a five phase PMSM for aerospace, EV and ship propulsion applications. Additionally, [14] applied hybrid modelling to enable real time implementation of hardware-in-the-loop simulation. Similarly, [10] constructed a PMSM hybrid model to aid in the evaluation of dynamic machine

The associate editor coordinating the review of this manuscript and approving it for publication was Ning Kang.

performance and the development of high performance control algorithms. Furthermore, a condition monitoring study in [8] applied hybrid modelling to explore the detection of a stator turn fault.

A primary hurdle in developing the hybrid FEA-dq model is the significant amount of time needed for its construction [8]. This is due to the requirement to pre-calculate the magnetic circuit behaviour for the full range of d-q current and rotor position variations of interest, which is a highly time consuming process that can take weeks or more depending on the geometry and the problem analysed. While constructing hybrid FEA-dq models is time consuming due to the FEA pre-calculation of LUT data, these models offer rapid execution times with high fidelity once they are established. To put that into context, the hybrid FEA-dq model described in this paper can simulate a transient drive cycle lasting 120 seconds, sampled at 10 kHz, in approximately 7 minutes. In contrast, performing the same simulation in a purely dynamic FEA environment could take several months.

An area that has not received adequate attention is the impact of LUT construction parameters on the accuracy of prediction of electrical and mechanical signals in both the time and frequency domains within these models. Gaining insight into how the specification of FEA pre-calculations and the features of their processing into suitable LUTs affects the hybrid model error magnitude has the potential to reduce the computational workload and expedite the construction process, for a desired level of accuracy, but has not been addressed in literature. While limited work [6], [7], [9], [15] acknowledges how certain LUT building components such as data interpolation techniques compare in terms of accuracy, these authors do not explore the appropriate selection of the mechanical rotor step and the current step in FEA pre-calculation, nor the factors that determine and influence their size. The research in [8] and [16] utilised the hybrid FEA-dq model but did not explain the choice of applied current and rotor step.

This paper investigates the extent to which the parameters used in constructing the model LUTs influence the accuracy and fidelity of dynamic simulations in both the frequency and time domains, as well as the development time. The underlying aim is to provide greater clarity regarding the setup of key features of hybrid FEA-dq models and thus an increased confidence in their utilisation. Section II presents the details of hybrid d-q model architecture and construction. Section III establishes a hybrid d-q model of an exemplar commercial surface mount PMSM design, used as a test machine in this study. Section IV explores the influence of FEA pre-calculation rotor step size and the motor current step size on the accuracy of model predictions and execution time requirements through direct comparison of simulation results to extract the general rules for effective step selection. In section V part B, model predictions for the finest rotor step size are compared in time and frequency domain against measurements obtained from a purpose-built laboratory test system to validate the hybrid FEA-dq dynamic model. Part C focuses on transient analysis, aiming to illustrate how well the finest rotor step size and current step size in the hybrid FEA-dq model can accurately represent electromagnetic and mechanical signals during a dynamic drive cycle (FTP75), which simulates urban driving conditions for a car.

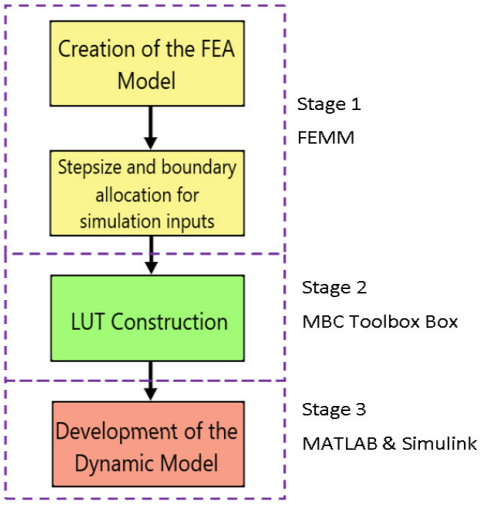

FIGURE 1. Construction process of the hybrid FEA-dq model.

II. HYBRID FEA D-Q MODEL ARCHITECTURE AND CONSTRUCTION

A. HYBRID FEA D-Q MODEL DEVELOPMENT

The development of a hybrid FEA-dq model can be classified into three stages – constructing the FEA model and pre-calculating the current / flux linkage data, configuring the LUTs with a defined interpolation technique and resolution, and lastly composing the dynamic model, as illustrated in Fig. 1. During the initial stage, the Finite Element Method Magnetics (FEMM) FEA software environment was chosen as it has the capacity to solve low frequency electromagnetic problems effectively on a two dimensional plane [17], is open source and has the ability to execute script from MATLAB. Using FEMM, in the initial stage of the construction process a detailed 2-D representation of the machine geometry is formulated and solved in multiple simulations. Each solution is for a specific combination of rotor position and dq-currents, which are mapped to the abc coil currents, and solved as a static 2D current-fed case. A MATLAB script was utilised to systematically execute the FEA model for the set of id and iq current combinations and rotor positions.

The second stage of the construction process involves the inversion of the FEA predicted data by expressing the currents id and iq as functions of flux linkages λ_d and λ_q as well as the rotor angle θ_m, i.e. $i_{d,q}(\lambda_{d,q}\ \theta\text{m})$. To establish how the discrete points from the FEA simulation distributed across the d-q plane are interconnected, and thus ensure adequate resolution of the LUTs, a surface is fitted to each individual 2-D d-q space that represents the current - flux linkage relationship for a specific rotor angle. The process of interpolation and construction of 2-D LUTs was carried

out using the MATLAB's Model Based Calibration (MBC) toolbox [18]. The merging of the 2-D LUTs into a single 3-D LUT also indexed by rotor angle was performed using MATLAB.

The final stage of constructing the hybrid model involves configuring the d-q model architecture in Simulink using PM machine dynamic voltage and mechanical torque equations. The model is expressed in terms of flux linkages which serve as inputs alongside the mechanical angle to the 3-D LUTs. The flow chart representation in Fig. 1 illustrates all major the steps involved in constructing a hybrid model as discussed above. The main emphasis of this research is placed on the first stage, which involves determining the range and resolution of the LUTs. Prior to running the FEA simulation, it is necessary to determine the values for the rotor step and the current step. These selections will ultimately determine the overall simulation time and accuracy.

B. FEA MODEL CONSTRUCTION

FEMM was used to establish a magnetostatic FEA electro-magnetic model of the examined PMSM which was then used to perform the simulation of the operation conditions of interest as detailed in section III. Only the simulation with the finest considered current step (1A) and rotor step angle (1°) was performed. Larger current and rotor increments were obtained by down-sampling the detailed dataset, giving integer multiples of 1A and 1°. The pre-calculated current range was set to ±10A for iq, and ±3A for id, and performed for 120 different mechanical rotor positions, as detailed in section III. As a result a total of 17,640 individual FEA model simulations were executed. During this process, appropriate material types are assigned to all the physical bodies and a simulation boundary that encompasses the entire model structure is established. All the objects within the model were meshed using an automated mesh generator giving a 119 000 node density within the machine's stator and rotor geometry. A higher density mesh was tested (200 000 nodes), but did not result in any noticeable alterations in the computed flux linkages. Typically, the computation time for each individual solution averaged ≈150 seconds on a computer equipped with an Intel core i7-5960X processor clocked at 3.00 GHz with a RAM size of 32.0 GB. The extensive set of 17,640 computations required ≈30 days of continuous run time to complete. This long computational time could potentially be substantially diminished by understanding the impact of relevant step size choices on the precision of the dynamic model.

C. LUT DESIGN

Within this simulation model, the primary purpose of the LUT is to store the id and iq current data, which can be retrieved by indexing the appropriate inputs for flux linkages in the d-q axes and the mechanical rotor angle. A separate study [15] examined the impact that interpolation and extrapolation algorithms have on the accuracy of the LUTs, identifying

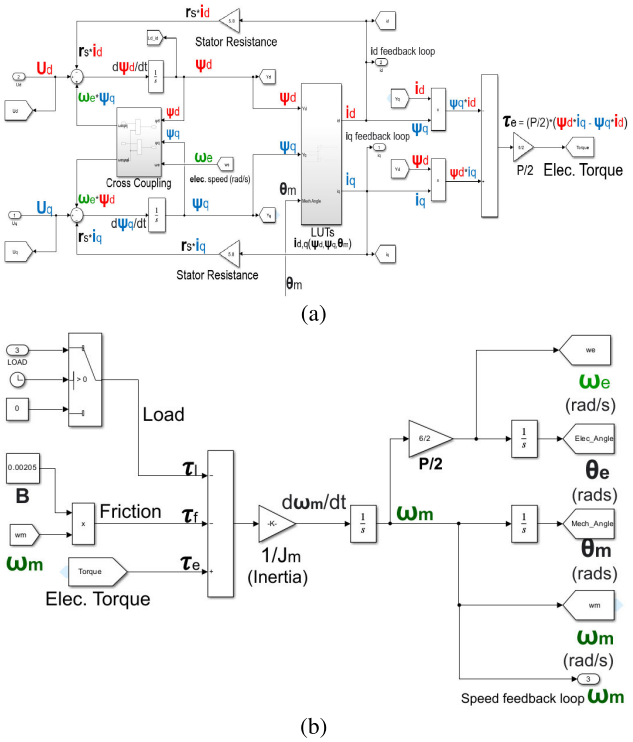

FIGURE 2. Dynamic model of the 1.1kW PMSM in Simulink (a) Electro-magnetic part. (b) Mechanical part.

the kernel functions from the Gaussian Process model and the Interpolation Radial Basis Function (RBF) model as the interpolation methods that provide the lowest average error. For the PMSM in Section III, [15] determined that optimal resolution for each 2D LUT size would be 80 by 80, resulting in an error margin between the desired value (FEA generated) and the actual value of less than 0.15%. These findings [15] were used in this study to facilitate high accuracy LUT construction for all the simulation models considered.

D. DYNAMIC MODEL

The dynamic model which incorporates the LUTs was constructed using the d-q voltage dynamic equations as expressed below in equations (1) and (2):

$$\frac{d\lambda_d}{dt} = u_d - R_s i_d + \lambda_q \omega_e \tag{1}$$

$$\frac{d\lambda_q}{dt} = u_q - R_s i_q - \lambda_d \omega_e \tag{2}$$

where the $\lambda_{d,q}$ parameters represent the flux linkages in the d-q axis, the $u_{d,q}$ terms signify the voltages in the d-q axis, the R_s term represents the stator resistance, and the ωe term represents the electrical angular speed. Numeric integration of (1) and (2) gives flux linkages in the d-q axis that along with the mechanical rotor angle form inputs into two 3-D LUTs, one for i_d and the other for i_q, as shown in equations (3) and (4).

$$i_d = i_d(\lambda_d, \lambda_q, \theta_m) \tag{3}$$

$$i_q = i_q(\lambda_d, \lambda_q, \theta_m) \tag{4}$$

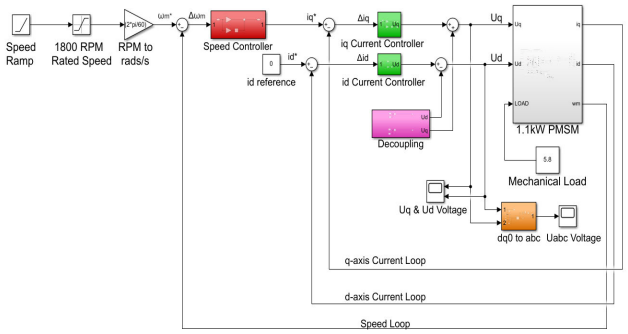

FIGURE 3. Integration of the 1.1kW PMSM with standard vector control.

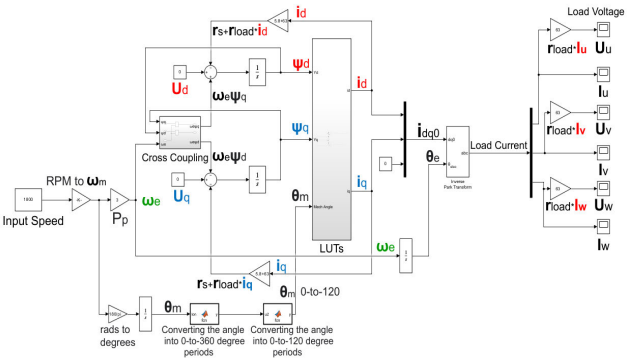

FIGURE 4. Generator model of the 1.1kW PMSM connected to a balanced resistive load.

The electromagnetic torque and mechanical speed of the PMSM machine are mathematically described by equations (5) and (6):

$$T_e = \frac{N_p}{2}(\lambda_d i_q - \lambda_q i_d) \tag{5}$$

$$\frac{d\omega_m}{dt} = \frac{1}{J_m}(T_e - T_L - B\omega_m) \tag{6}$$

where T_e denotes the electromagnetic torque, N_p represents the number of poles, ω_m signifies the mechanical speed, J_m represents the inertia constant of the machine, T_L denotes the load torque and B represents the viscous friction coefficient. Integration of (6) can then be used to derive the electrical speed and angle. (1)-(6) assume a constant power Clarke transformation and motoring convention. The zero sequence is neglected since most PMSM machines have an isolated star connection. In Fig. 2, part (a) depicts the electromagnetic part of the 1.1kW PMSM motoring simulation circuit diagram in Simulink, based on equations (1)-(4), whereas part (b) represents the mechanical part of the circuit, derived from equations (5)-(6). Fig. 3 shows the integration of the machine model into the FOC strategy. The current and speed controller gains were obtained using the auto-tune feature of the commercial UniDrive SP1405. This approach ensured that both the simulation and the test rig, described later, have identical controller parameters. The inverter is modelled with switch-averaged voltages; as is usual for motor dynamic modelling, full switching detail is omitted for computational speed. Fig. 4 displays the Simulink dq model of the 1.1kW PMSM set up as a standalone generator connected to a balanced resistive load. The only input parameter to the model is the mechanical speed. The electromagnetic torque is defined by the resistive load imposed on the machine. This circuit is used to validate the developed hybrid FEA-dq models with different rotor angle against obtained measurements from the test rig shown in Fig. 12 (a) under steady state conditions described in Section V.

III. TEST MACHINE DESIGN AND STEP SIZE SELECTION

Table 1 presents the datasheet parameters and measured geometry of the commercial Lafert HPS 711800 23, surface mount PMSM in this study to determine the rotor step size and current step size selection ranges of interest for FEA pre-calculations. To capture the air-gap field distribution including slotting and rotor geometry effects, as presented in Table 1 and Fig. 5(a), the stator slot pitch and tooth pitch of 2.75° and 6.48° respectively set resolution and criteria for the rotor angle step. Due to the symmetry of the stator and the rotor magnetic circuits, stepping the 6-pole rotor over a single electrical cycle, which equates to 120° mechanical, was sufficient. This reduced the total required FEA simulation time by two thirds compared to executing a full 360 degree simulation run. Stepping the rotor over half an electrical cycle (60° mech.) was not feasible due to asymmetry in the winding configuration, as illustrated in Fig. 5(b) which shows the windings' composition and individual coil turn number and pitches (in multiples of the stator slot pitch). Applying a mech. rotor stepping angle of 30°, for example, would only capture the current to flux linkage relationship at four specific spatial points per electrical cycle, thereby overlooking many slotting harmonics and their influence on motor electromagnetics, and causing aliasing effects. A minimum of 2 samples per cycle are required for accurate for spatial harmonic observation, hence with 30 degree step only up to the 2nd harmonic can be observed. A smaller step size, like 10 degrees, allows seeing up to the 6th harmonic, but can introduce errors due to potential aliasing from higher harmonics like the 7th, distorting lower frequencies. The machine nominal dq current of 3.9 A was used as a guide in determining the size and the range of current stepping at the FEA pre-calculation stage. A higher current step size would generally result in a lower fidelity and fewer saturation characteristics being captured. Therefore, at the FEA pre-calculation stage, current steps of 1A and 3A in the d-q domain were chosen for evaluation at FEA pre-calculation stage. To cater for both the motoring and generating modes of operation, the upper and lower boundary limits for i_q and i_d were defined as ±10 A and ±3 A, respectively. The limit on i_q was set high to account short-term current transients above the rated level, i.e. a rapid speed/load change. The upper and lower limits for i_d were set to ±3 A to cover the operating points near the normal operating condition of zero i_d, neglecting field weakening. The current step in the FEA is

TABLE 1. 1.1kW PMSM design features and rated values.

Parameter	Value
Part Number	HPS 711800 23
Phase Count	3
Pole Number	6
Rated Power	1.1 kW
Rated Current	2.3 A rms
Rated Speed	1800 RPM
Rated torque	5.8 Nm
BEMF	303 V rms
ψ_m	0.39 Wb
Phase Resistance	5.8 Ω
Phase Inductance	24 mH
Stator Slot Count	39
PM Pitch	49^o mech.
Stator Tooth Pitch	6.48^o mech.
Stator Slot Pitch	2.75^o mech.
Air-gap Inner Radius	32.26 mm
Air-gap Outer Radius	33.53 mm
Stator Coils Wire Type	24 AWG Copper
Stator/Rotor Material	430 Stainless Steel
Rotor Magnet Type	NdFeB 35 – grade
Air-gap Material	Air

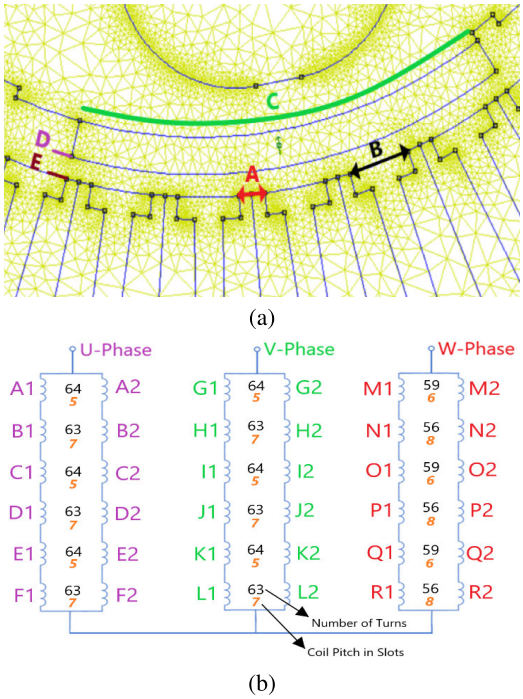

FIGURE 5. Machine geometry and winding. (a) Stator and rotor features: A = Stator Slot Pitch, B = Stator Tooth Pitch, C = PM Pitch, D = Air-gap Inner Radius and E = Air-gap Outer Radius. (b) Phase winding layout.

dependent on the linearity of the magnetisation curve of the machine's electrical steel.

IV. LUT BUILD PARAMETER SENSITIVITY STUDY

This section applies the principles presented in section III to explore the impact on the time and frequency domain response of the dynamic simulation by selecting different values for the two main build parameters of the LUTs – the mechanical rotor step and the current step. The hybrid FEA d-q model dynamic simulation results are subsequently quantified to characterise the associated error magnitude. All the simulated scenarios correspond to the machine being operated under nominally healthy conditions. The findings of this analysis are then summarised by evaluating the trade-offs between the precision of the dynamic model, the mechanical rotor step, current step, model development time, computational time and other relevant factors.

A. ROTOR MECHANICAL ANGLE STEPPING

Six hybrid FEA-dq models were constructed with 80 × 80 d-q current LUTs having a mechanical step size of 1°, 2°, 3°, 10°, 20° and 30°. They all shared a common current step value of 1A since the objective of this part was to investigate the impact of mechanical stepping on the dynamic simulation results. All six models were subjected to identical conditions: a constant rated speed of 1800 RPM, rated load of 5.8Nm, an identical simulation duration and a consistent Simulink solver (Runge Kutta 45) time step of 10 μs. The results were analysed using MATLAB FFT computations with a frequency resolution of 0.1Hz. The modelled phase current at each of the considered step sizes is shown in Fig. 6(a) and (b) in time domain and Fig. 6(c) and (d) in frequency domain.

Conventional field-oriented control generates sinusoidal reference currents, but the higher resolution hybrid model captures disturbances in the currents due to back EMF harmonics and unbalanced windings. Fig. 7 shows that the errors due to mechanical stepping only become apparent in the time domain when the step size is $\geq$10°. Fig. 3(a) indicates there is no significant difference observed when employing low step sizes (1, 2 and 3 mechanical degrees); the difference in the Total Harmonic Distortion (THD) value between the three was found to be lower than 0.3%, as shown in Table 2. The current waveform is seen to become increasingly more sinusoidal with the mechanical step increase due to fewer spatial harmonic effects being captured, as presented in Fig. 7(b). As observed in Fig. 6(c) the frequency spectrum reveals observable differences around even harmonics, which exhibit very small magnitudes. The presence of these even harmonic components can be attributed to the unbalanced winding architecture of the test machine. Fig. 6(d) shows that larger step values are missing these 2nd harmonic components and introducing false additional inter-harmonics, which are non-integer multiples of the fundamental [20], [21].

To numerically quantify the changes introduced by individual harmonics and their impact on waveform distortion in all six different mechanical step size scenarios, Table 2 compares the simulated phase U current harmonic components up to the 11th harmonic for each of the mechanical step sizes.

From Table 2, it becomes apparent that the most harmonic components diminish as the mechanical step size gets larger and the total harmonic distortion (THD) value decreases substantially. The greyed out cells show that there are insufficient samples per cycle to capture this harmonic correctly. In summary, the current fundamental component can be predicted consistently with an error of no more than 0.5% using any mechanical step size up to 20° for

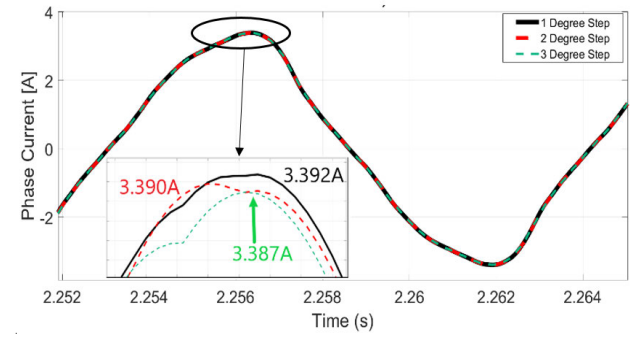

(a)

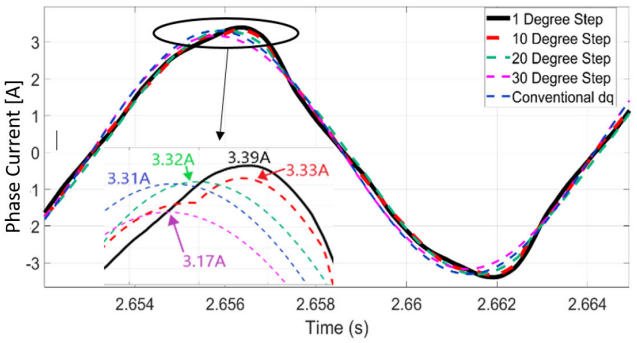

(b)

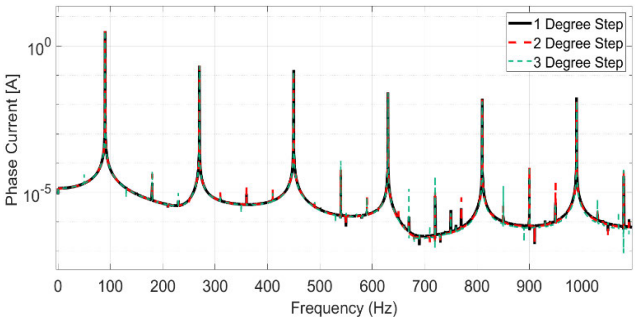

(c)

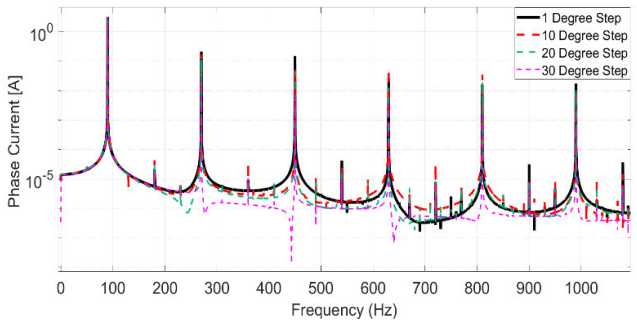

(d)

FIGURE 6. Phase U current under nominal operating conditions. (a) Time domain under mechanical rotor step of 1, 2, 3, 10, 20 and 30 degrees. (b) FFT under mechanical rotor step of 1, 2 and 3 degrees. (c) FFT under mechanical rotor step of 1, 10, 20 and 30 degrees.

the examined machine geometry. However, a mechanical step size of 30° will result in an error of 1.33% which is significantly greater. Fig. 7 illustrates the propagation of errors in the 1st, 3rd, 5th and 7th order harmonics for

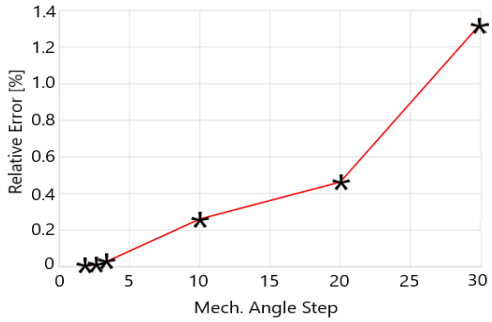

(a)

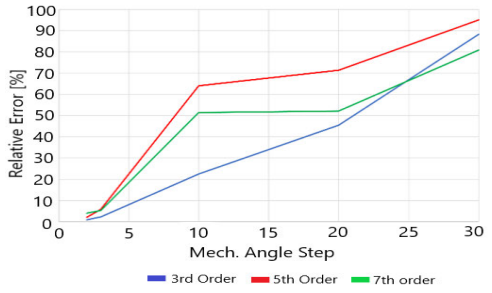

(b)

FIGURE 7. Phase Current error relative to the 1 degree rotor step simulation. (a) Fundamental (b) 3rd, 5th and 7th harmonic.

mechanical step sizes of 2, 3, 10, 20 and 30 degrees relative to the harmonic components obtained using a mechanical step size of 1°. Only a 1 degree step size ensures two samples per slot. In general, the relative harmonic magnitudes decrease for larger step angles. The exception is the 7th harmonic at 10°, which is reinforced by aliasing of the 9th harmonic, due to sampling at 12 times per electrical cycle.

The voltage waveforms shown in Figs. 8(a) and 8(b) follow a similar pattern to the current, exhibiting reduced distortion in the time domain and lower harmonic content in the frequency domain as the step angle increases but with more inter-harmonics, as illustrated in Figs. 8(c) and 8(d) and summarised in Table 3. Similar to the current waveforms, differences in the time domain among voltage waveforms become more evident when the rotor step exceeds 10 degrees. Regarding the fundamental voltage component, the error remains below 0.31% for rotor steps up to 20 degrees. However, a 30-degree step shows a significant increase in prediction error for the fundamental component, approximately 1.97%, considerably higher than errors observed with other rotor steps.

Cogging torque is produced by the interaction between the PM poles on the rotor and the iron teeth in the stator laminations. As the rotor rotates, it tries to align with the stator teeth, which offer the path of least reluctance. An external force is required to break this alignment. This machine characteristic was examined using FEMM to determine how much detail of the cogging torque ripple could be captured at different rotor step sizes. This was achieved by rotating the rotor through one electrical pole, 120 degrees, without injecting any current into the windings. Fig. 9 shows

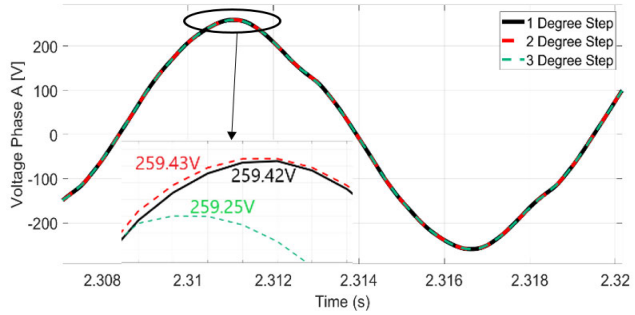

(a)

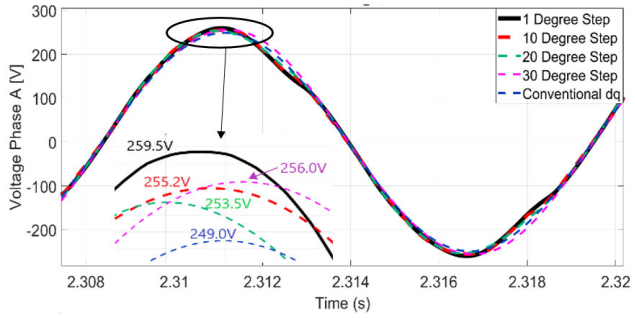

(b)

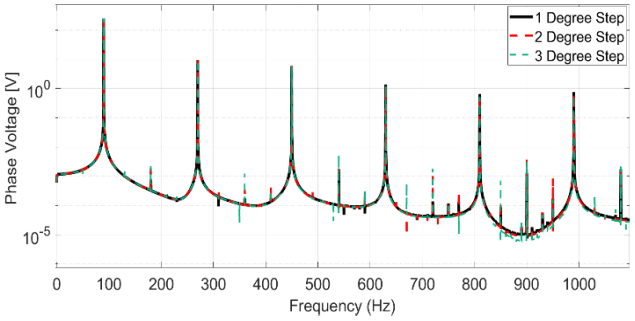

(c)

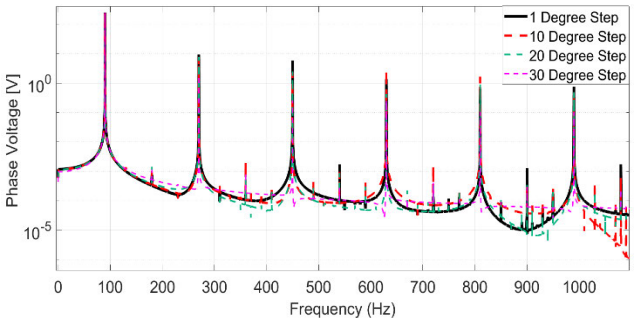

(d)

FIGURE 8. Phase U voltage under nominal operating conditions. (a) Time domain under mechanical rotor step of 1, 2 and 3 degrees. (b) Time domain under mechanical rotor step of 1, 10, 20 and 30 degrees. (c) FFT under mechanical rotor step of 1, 2 and 3 degrees. (d) FFT under mechanical rotor step of 1, 10, 20 and 30 degrees.

the results for the cogging torque, where part (a) displays the relative difference between low incremented rotor steps whilst part (b) shows it for high incremented rotor steps.

TABLE 2. Phase current harmonics magnitudes in A for different mechanical step size under nominal load and speed conditions.

Harmonic No.	1° Step	2° Step	3° Step	10° Step	20° Step	30° Step
1^{st}	3.229	3.229	3.229	3.221	3.214	3.186
3^{rd}	0.212	0.210	0.207	0.165	0.116	0.024
5^{th}	0.151	0.149	0.143	0.055	0.043	0.007
7^{th}	0.026	0.025	0.025	0.054	0.013	0.005
9^{th}	0.016	0.018	0.013	0.035	0.020	0.003
11^{th}	0.017	0.016	0.013	0.010	0.010	0.002
THD (%)	8.14	8.04	7.80	5.75	3.92	0.83

TABLE 3. Phase voltage harmonics magnitudes in V for different mechanical step size under nominal load and speed conditions.

Harmonic No.	1° Step	2° Step	3° Step	10° Step	20° Step	30° Step
1^{st}	251.192	251.204	251.209	251.464	251.966	256.233
3^{rd}	9.480	9.415	9.308	7.783	7.754	1.840
5^{th}	5.961	5.851	5.639	2.293	2.534	0.257
7^{th}	1.388	1.335	1.314	2.818	0.427	0.252
9^{th}	0.646	0.595	0.519	1.652	0.889	0.105
11^{th}	0.757	0.708	0.591	0.500	0.491	0.103
THD (%)	4.51	4.46	4.38	3.48	3.27	0.73

As noted in Table 1, the stator slot pitch is 2.75°. For this reason, only the 1 degree and 2 degree rotor step size simulations were able to accurately detect the effect of all the slots. The 3 degree step simulation missed a few slots because it covered more than one slot per rotor step. In contrast, the 10 degree, 20 degree, and 30 degree rotor step size simulations completely missed this detail, as they spanned several slots per step. Therefore, with larger rotor step sizes, the variations in flux linkages caused by slot effects cannot be captured correctly, leading to an incomplete representation of torque ripple under dynamic simulation conditions.

B. CURRENT MAGNITUDE STEPPING

The impact the current magnitude stepping has on model predictions was investigated by constructing two hybrid FEA datasets. Both incorporated the finest rotor step of 1° but differed in the current step using 1 A and 3 A respectively and aimed to assess representation of saturation effects. The two LUTs were subjected to identical operating conditions to the tests in Section IV-A and were constructed using the same 80 by 80 resolution.

Fig. 10 presents the comparison of the phase current predictions: Fig. 10(a) demonstrates there is a negligible distinction between the two time-domain waveforms, which exhibit the same shape and peak values. Their FFT spectra in Fig. 10(b) however reveal that while the odd harmonic components of the current exhibit closely similar magnitude, there is a significantly amplified value for the even harmonic components for the simulation response of the 3A step. The magnitude of the harmonic components in Table 4 clearly demonstrates minimal disparity between the fundamental current response of 1 A step and the 3 A step of less than 0.06%. The discrepancy between the highest order harmonic examined, the 11th harmonic, is merely 1.72%.

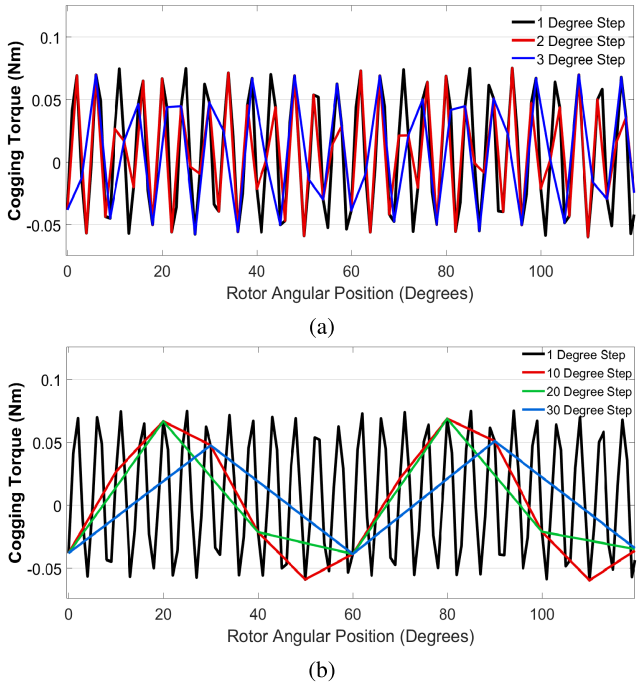

FIGURE 9. Cogging torque in FEMM. (a) Low rotor angle increments (b) High rotor angle increments.

TABLE 4. Numerical values of FFT components for the phase current in A under nominal load and speed conditions. Current Stepping.

Harmonic No.	1 A Step	3 A Step
1^{st}	3.229	3.228
3^{rd}	0.212	0.212
5^{th}	0.152	0.148
7^{th}	0.026	0.020
9^{th}	0.016	0.016
11^{th}	0.017	0.017
THD(%)	8.15	8.08

Model predictions for the voltage signals in the current step cases considered are shown in Fig. 11, showing consistent effects to those observed in the current.

Fig. 11(a) data reveal no discernible difference in the time domain between the 1 A step and 3 A step simulations, while the frequency domain data shown in Fig. 11(b) shows the main distinguishable difference as the amplified magnitude of the even and inter harmonic components. The difference between some of these even harmonics can be as high as three decades (i.e. from 10e-4 to 10e-1). When compared to one another, the odd harmonic components however display reasonable accuracy. The difference between the fundamentals for example, is merely 0.015% whereas between the 11th order harmonics it is 8.93%. Table 4 contains the odd harmonic values for the current waveform and Table 5 for the voltage waveform.

V. EXPERIMENTAL RESULTS

A. TEST RIG DESCRIPTION

A laboratory test system was developed for experimental validation, as shown in Fig. 12(a), comprising the 1.1kW

TABLE 5. Numerical values of FFT components for the phase voltage in V under nominal load and speed conditions. Current Stepping.

Harmonic No.	1 A Step	3 A Step
1^{st}	251.192	251.229
3^{rd}	9.480	9.616
5^{th}	5.961	5.857
7^{th}	1.388	1.132
9^{th}	0.646	0.597
11^{th}	0.757	0.690
THD(%)	4.51	4.52

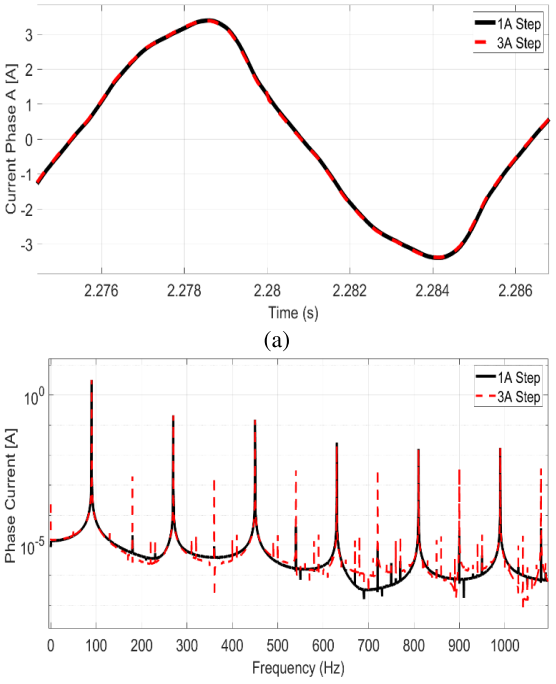

FIGURE 10. Comparison of the phase current signal under nominal conditions. (a) Time domain of the phase current under current step of 1A and 3A. (b) FFT of the phase current under current step of 1A and 3A.

PMSM described in Table 1. For the steady-state tests, the machine was operated in the generating mode. The PMSM was mechanically coupled to a brushless AC servo motor with a rated torque of 12.4 Nm and a speed of 3000 RPM, which served as a prime mover. The servo was driven in a speed control loop using a commercial UniDrive SP1405. By using a variable power resistor bank configured in a star formation as an electrical load, the 1.1kW PMSM was tested at full load conditions while operating at the nominal speed of 1800 RPM. Measurements of both current and voltage were sampled at 100 kHz. A Digital Oscilloscope (LeCroy WaveSurfer 434 350MHz) and current probe (LeCroy CP150 0.01 V/A) were used.

The transient mode of operation in the motoring mode was performed through the use of closed loop field oriented control. The 1.1kW PMSM was driven by a UniDrive SP1405 in the speed control loop whilst the brushless AC servo machine acting as a load was driven by another UniDrive SP1405 in torque control. This is shown in Fig. 12(b).

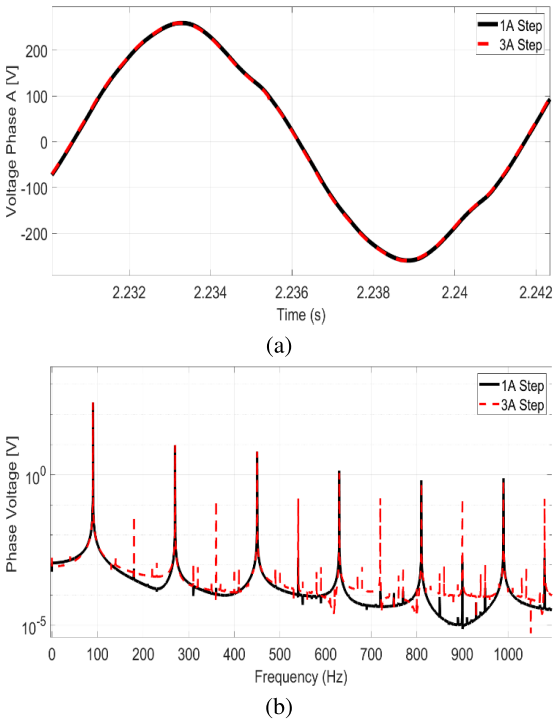

FIGURE 11. Comparison of the phase voltage signal under nominal conditions. (a) Time domain of the phase voltage under current step of 1A and 3A. (b) FFT of the phase voltage under current step of 1A and 3A.

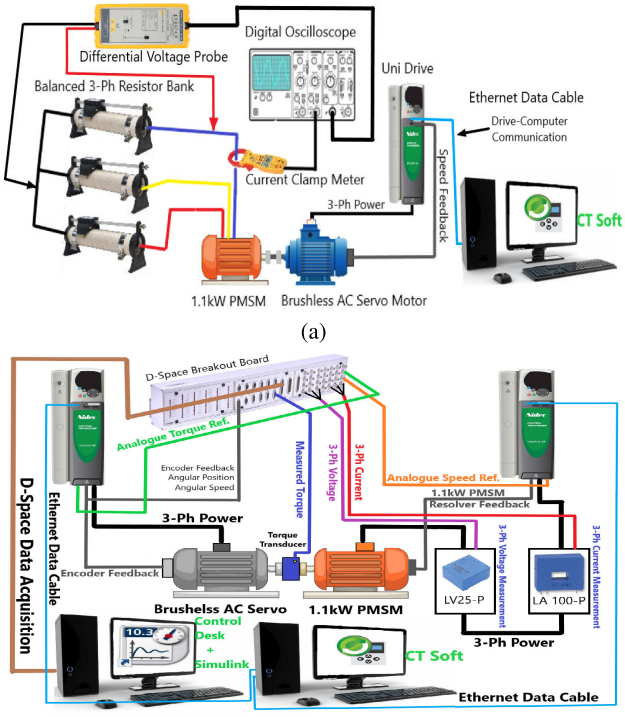

FIGURE 12. Experimental setup. (a) Test rig of the 1.1kW PMSM in the generating mode of operation. (b) Test rig of the 1.1kW PMSM in the motoring mode of operation.

An urban drive cycle for a car [22] was employed to determine the reference speed for operating the 1.1kW PMSM and the reference torque for controlling the AC servo load machine. These reference signals were scaled to ensure they remained within the specified speed and torque limits for both machines. By employing the dSpace interface platform, real-time measurements of encoder signals and all three-phase current voltage signals were captured using LA 100-P and LV25-P sensors followed by analogue low-pass RC filters with a cut-off frequency of 1592 Hz to attenuate the PWM switching noise. Currents in the d-q domain were exported as analogue outputs from the UniDrive and logged in dSpace. The speed of the machine was calculated using the 4096 line encoder position signals processed through a PLL loop with a damping factor of $\zeta = 0.9$ and natural frequency of $\omega = 20$, while the torque was obtained from the analogue output of the in-line TorqSense ST transducer. All dSpace signals were sampled at 10 kHz throughout the whole drive cycle.

B. STEADY-STATE VALIDATION

The machine was first operated as a standalone generator to ensure signals are purely defined by machine electro-magnetics rather than the inverter switching or control. Fig. 13(a) compares the predicted and observed time-domain current signals under standard operating conditions, revealing minimal disparities between the measured and simulated signals using simulation models with rotor step degrees of 1°, 2°, and 3°. However, noticeable differences in the time domain become more apparent when using rotor step sizes of 10° or higher in the simulation model, as shown in Fig. 13(b). This is due to the simulation models with larger rotor step sizes not capturing higher-order harmonics, resulting in waveform becoming more sinusoidal. Figs. 13(c) and 13(d) show the corresponding voltages, with a similar trend with step size.

The spectral domain results for currents and voltages in Fig. 14, illustrate the similarities between measured and simulated values. Note that part IV that compared frequency domain values during motoring operation in a speed control loop and this test looks at the generating mode without any controller, giving lower values for both the THD and harmonic components. All charts in Fig. 14 demonstrate a good match on frequencies, including even harmonics and a close match on fundamental magnitudes. Additionally, accurate trends can be observed in odd harmonics and THD. One drawback of the measurement is the elevated noise floor originating from the experiment, attributable to the limitations in equipment resolution. Tables 6 and 7 provide quantified magnitude values for all odd harmonics up to the 11th harmonic. All the simulation models have accurately predicted the magnitude of the fundamental harmonic within 1 %.

Disparities between other odd harmonic components for all the simulation models are larger, which affects the value of the THD. As shown in Tables 6 and 7, the THD for voltage and current decreases with the increase in the rotor step angle.

TABLE 6. Numerical values of FFT components for the phase current in A under nominal load and speed conditions. Generating mode of operation.

Harmonic No.	1° Step	2° Step	3° Step	10° Step	20° Step	30° Step	Measured
1^{st}	3.313	3.313	3.313	3.316	3.323	3.325	3.306
3^{rd}	0.127	0.127	0.125	0.098	0.026	0.062	0.065
5^{th}	0.090	0.088	0.085	0.038	0.029	0.014	0.028
7^{th}	0.004	0.004	0.003	0.037	0.011	0.011	0.004
9^{th}	0.009	0.008	0.007	0.023	0.006	0.006	0.005
11^{th}	0.012	0.012	0.010	0.007	0.007	0.005	0.006
THD (%)	4.721	4.686	4.578	3.438	1.249	1.954	3.190

TABLE 7. Numerical values of FFT components for the phase voltage in V under nominal load and speed conditions. Generating mode of operation.

Harmonic No.	1° Step	2° Step	3° Step	10° Step	20° Step	30° Step	Measured
1^{st}	208.70	208.70	208.70	209.90	209.37	209.48	206.89
3^{rd}	8.021	7.971	7.890	6.201	1.622	3.896	4.275
5^{th}	5.686	5.571	5.372	2.368	1.836	0.874	1.511
7^{th}	0.281	0.257	0.207	2.346	0.676	0.666	0.063
9^{th}	0.560	0.521	0.426	1.459	0.380	0.395	0.255
11^{th}	0.794	0.734	0.644	0.443	0.434	0.294	0.351
THD (%)	4.736	4.681	4.590	3.432	1.245	1.944	2.202

The only odd harmonic component except for the fundamental that has been accurately predicted in the current signal up to three decimal points is the 7th order harmonic. Conversely, the prediction accuracy of voltage harmonics was not as accurate. Disparities between the measured and simulated voltage signals in the frequency domain are visible in Figs 14(c) and 14(d), with the simulation over-predicting the peak values for all the odd harmonics, except the fundamental. The over prediction of harmonic magnitudes captured by the hybrid FEA-dq model likely originates from overlooking imperfections during dynamic model construction, such as asymmetry in one of the phases caused by variations in the number of turns and the coil pitch. Although these design aspects were integrated into the FEA simulation, the electromagnetic parameters representing them, specifically the current flux-linkage relationship relative to the rotor position, were converted into d-q equivalents for simplicity in LUT construction and alignment with the simulation's focus on operating the machine as a motor under vector field oriented control. As the controller operates within the d-q frame and assumes machine balance, there was no need for the simulation model to be built in the UVW phase domain. This is reflected in the zero sequence component of the simulated currents and voltages, which both add up to zero. In practice, this is not possible as one of the phases would need to generate greater BEMF to sustain the same current. Another potential source of error could arise from a minor imbalance in the three-phase power resistor bank, all calibrated using a voltage supply and an ammeter to ensure matched resistance. Additionally, the measuring equipment utilised for voltage and current readings presents another potential source of discrepancy. For instance, the voltage probe model TA041 from PICO may exhibit an offset of <+/ 5mV, a noise level of 0.7mV rms, and its AC performance

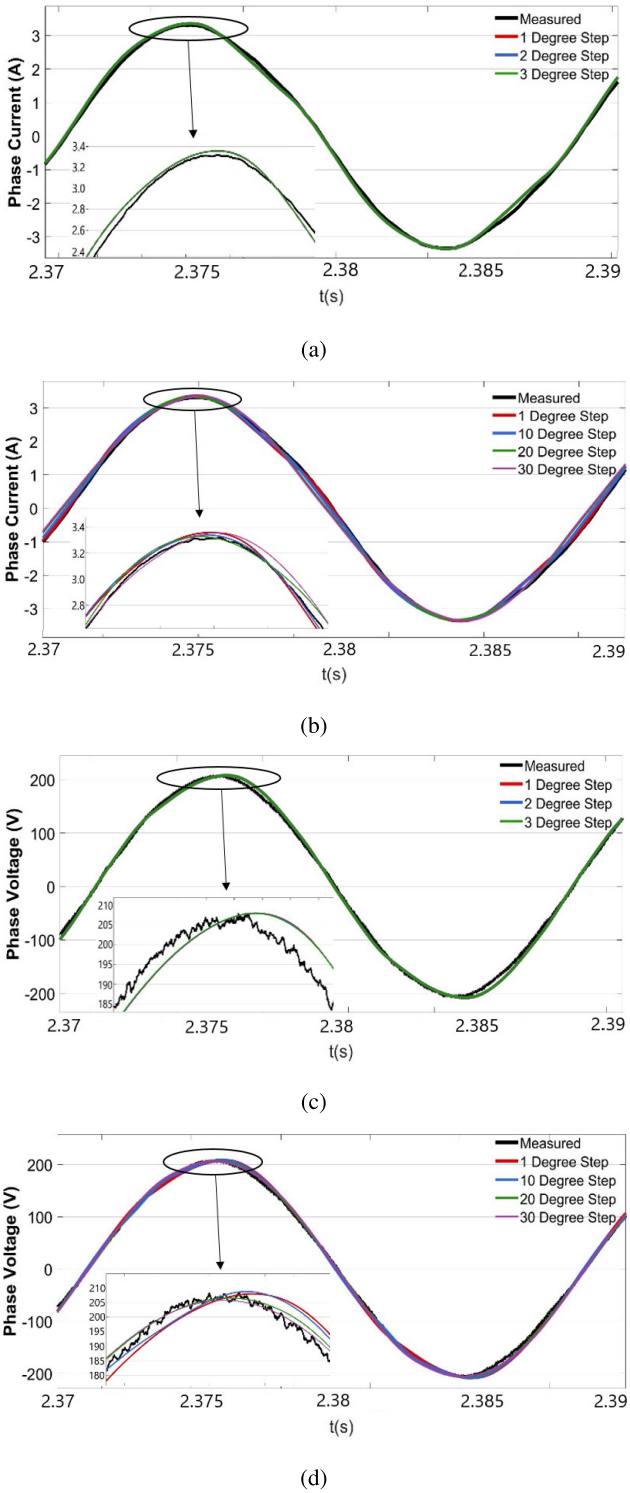

FIGURE 13. Experimental validation under generating mode of operation. Nominal operating conditions. (a) and (b) Phase current in time domain. (c) and (d) Phase voltage in time domain.

could vary within −3dB across its entire frequency range. Another source of error comes from the uncertainty about the type of steel used in the stator and rotor components. To address this problem, a trial and error approach was used

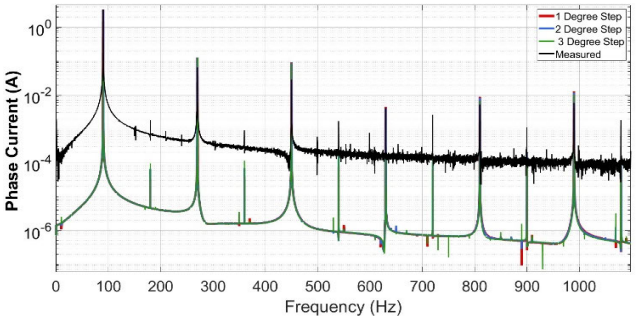

(a)

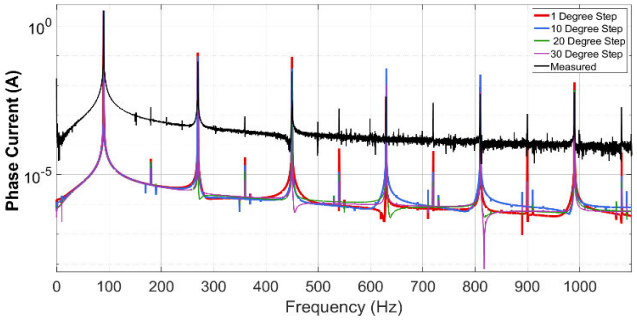

(b)

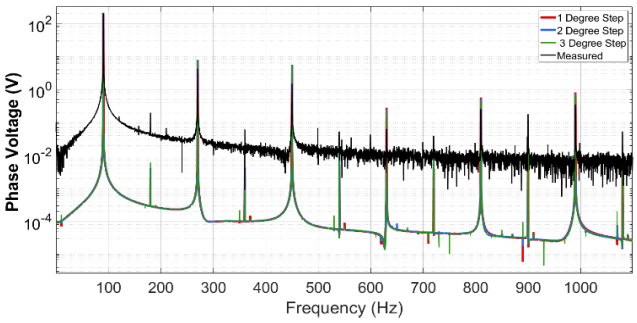

(c)

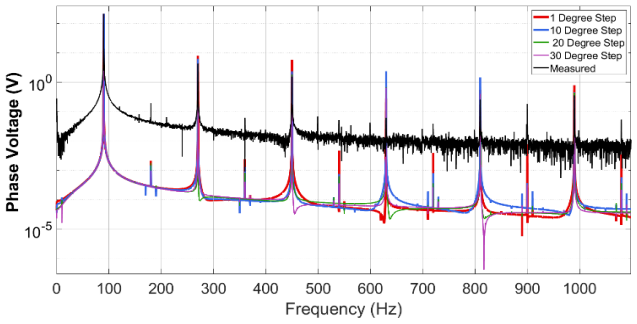

(d)

FIGURE 14. Experimental validation under generating mode of operation. Nominal operating conditions. (a) and (b) Phase current in frequency domain. (c) and (d) Phase voltage in frequency domain.

where steel materials with varying demagnetisation curves were evaluated. The selection process involved identifying the material that best matched the back EMF test results as well as the current and voltage measurements under nominal load conditions.

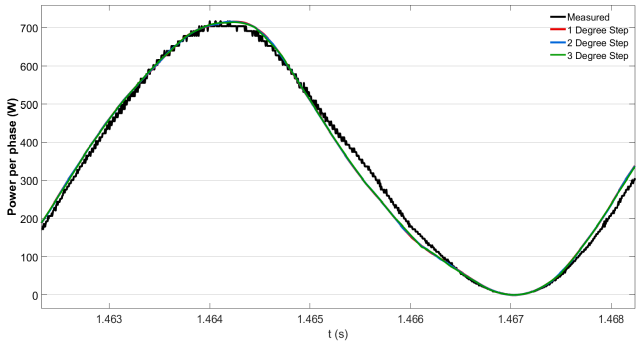

(a)

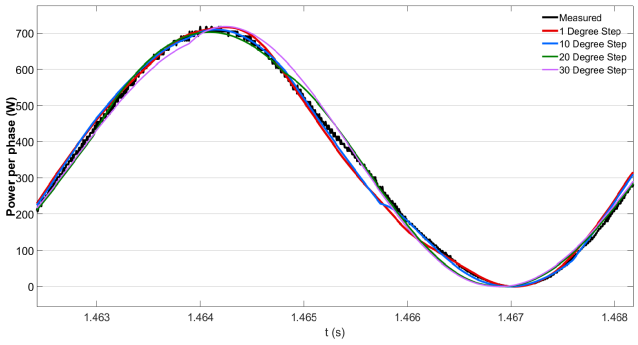

(b)

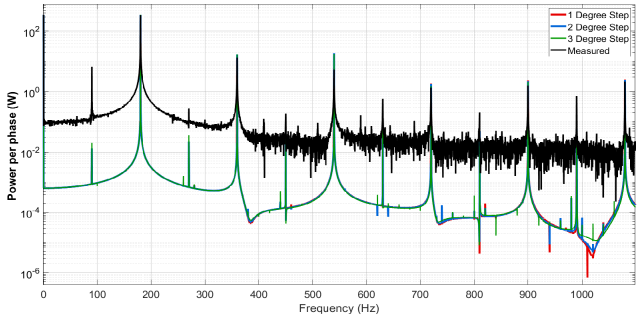

(c)

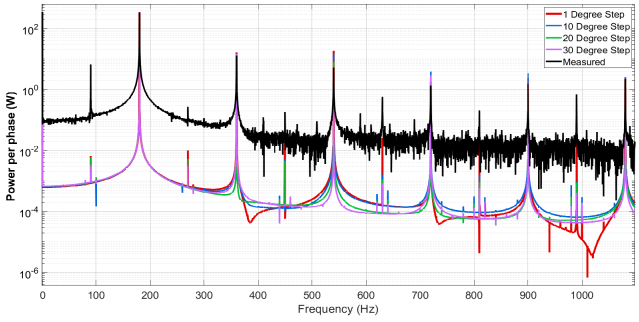

(d)

FIGURE 15. Active power per phase dissipated in the resistive load.(a) and (b) Active power in time domain. (c) and (d) Active power in frequency domain.

Figure 15 illustrates the time and frequency domains for the electrical active power per phase. Part (a) presents the

time domain signal for the low incremented rotor steps, while part (b) displays it for the high incremented rotor steps. Parts (c) and (d) depict the frequency domain for low and high incremented rotor steps, respectively. Since the active power is dissipated in the resistive load as I^2R, the waveform is elevated by its peak amplitude, creating a DC offset of 344 W and doubling the frequency of the fundamental. As anticipated, larger rotor angle increments produce waveforms that are more sinusoidal compared to those generated by smaller rotor angle increments. This is reflected in the reduced amplitudes of the 3rd and 5th harmonics. The 1 degree rotor step angle simulation yields values of 16.76 W and 18.71 W, whereas the 30 degree rotor step produces values of 14.60 W and 4.14 W, which is 12.9% and 77.9% lower.

C. TRANSIENT ANALYSIS

An urban vehicle drive cycle (FTP75) [22] was used to assess the impact of mechanical rotor stepping on the error in the model's predicted electromagnetic signals under continuously varying load conditions. Figs. 16(a) and 16(b) present a 120 second duration speed and torque drive cycle applied to the test rig in Fig. 12(b), operating under closed loop field oriented control. The speed profile served as an analogue input for the drive that controls the 1.1kW PMSM, while the load profile was applied as an analogue input to the drive operating the brushless AC Servo motor. The torque cycle, which was used as a load profile for the 1.1kW PMSM, was determined using the traction torque equation, which factors in multiple physical parameters relevant to the vehicle considered [23], such as the total mass including the payload, motor and wheel inertia, frontal area, gear differential ratio, gear efficiency, rolling resistance, and wheel radius. This investigation solely used the simulation model with the finest rotor step to assess its corresponding impact on the electromagnetic and mechanical signals in the time domain under dynamic conditions. As shown in Fig. 16(a), there is no noticeable difference in the speed signal between the measurement and simulation, throughout the entire cycle. Both were able to successfully track the speed profile, consisting of rapid acceleration and deceleration phases, as well as intervals of constant speed operation, resulting in a relative error of less than 0.1%. Fig. 16(b) illustrates the torque response, revealing both motoring and braking phases throughout the drive cycle. As illustrated, the simulated and measured responses align well during the motoring mode and also in the initial two braking phases, with a difference of less than 7% between them. The most notable difference between the two responses occurs in the final braking phase, with these distinctions being visible in the Figure.

The torque-generating current, i_q in Fig. 16(c), mirrors the pattern observed in the electromagnetic torque. The graph indicates a close match between the simulation and the actual measurement, with the most significant difference occurring during the final braking phase, corresponding to 0.3A in the power invariant d-q domain. Simulation models featuring larger rotor step sizes were also employed for this drive cycle, and it was discovered that using such models does not affect the DC component signals of speed or torque. However, it does influence their ripple content, which decreases in magnitude when simulation models with larger rotor steps are utilised. Similar to the torque signal, there are no variations in the fundamental value of i_q when employing simulation models with different rotor step sizes.

The only distinction noted is in the current ripple, which decreases as the rotor step size increases. The i_q current extracted from the measurement was influenced by the PWM switching noise produced by the inverter, which was not accounted for in the simulations. As a result, detailed comparisons regarding the current ripple between measurements and simulated values are not feasible. Fig. 17 shows a time domain plot of the phase voltage recorded at a specific point during the drive cycle. As indicated, the measurement and simulation agree on the peak voltage magnitude of 178 V. However, the main distinction lies in the harmonic distortion of the signals. The machine simulation does not include inverter's PWM switching effects, which are present in the measured signal and can obscure the machine's intrinsic electromagnetic characteristics. Figs. 18(a) and 17(b) illustrate the comparison between the measured and simulated controller voltages, U_d and U_q, respectively. The simulation successfully captures the voltage values during both motoring and rapid braking operating points, demonstrating its effectiveness in replicating test rig's operation. This shows that the simulation is capable of predicting the controller's behaviour across different points of operation, enhancing its utility in practical applications. Much like the current, the recorded voltage signal displayed a degree of switching noise. Nonetheless, it is worth noting that the differences between the measured signals and the simulated signals under transient conditions using the hybrid FEA-dq model are not substantial.Figs. 19(a) and 19(b) illustrate the variation in active and reactive power within the machine throughout the drive cycle. The peak power achieved is 750W, which corresponds to 68% of the machine's rated power. This is due to the fact that the peak load (5.8 Nm) and the maximum speed (1800 RPM) within the drive cycle do not coincide simultaneously, but occur at different intervals, as depicted in Figs. 16(a) and (b). The three negative regions in the active power chart indicate that the machine is sending power back to the drive system, due to regenerative braking. As observed, the reactive power remains at a low magnitude, below 75 VAR, for most of the driving cycle duration. However, it sharply increases to 230 VAR during rapid load transients and braking. There is a good agreement between the simulated and measured waveforms in both signals, although the largest discrepancies between the two occur during the final braking phase of the cycle, at t = 100s, with a maximum difference of 25% in active power (P) and 5% in reactive power (Q).

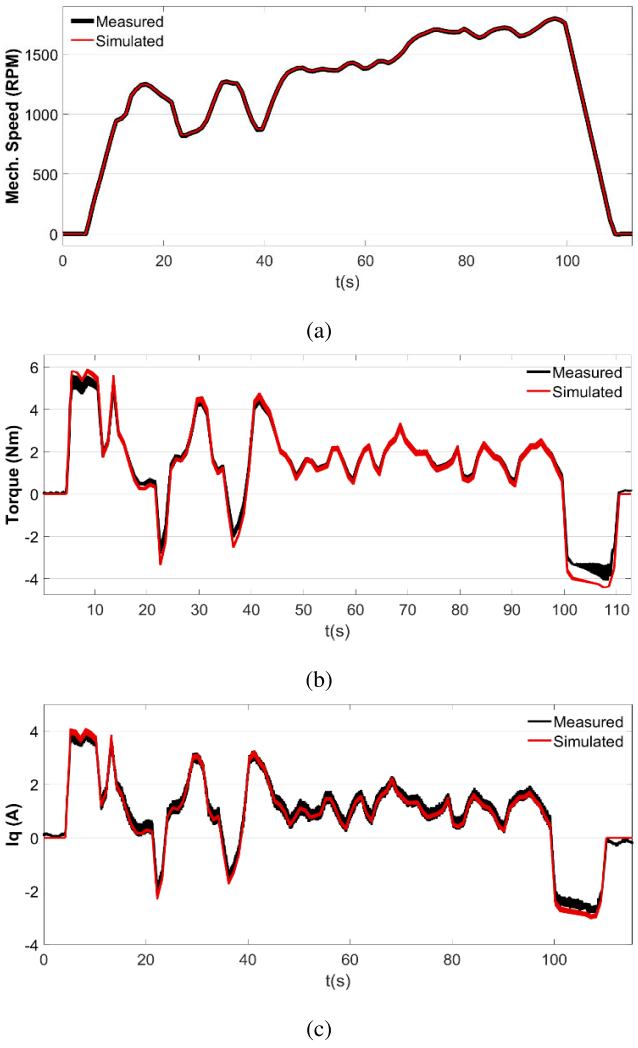

FIGURE 16. Experimental validation under urban drive cycle FTP75. (a) Speed. (b) Torque. (c) Iq Current.

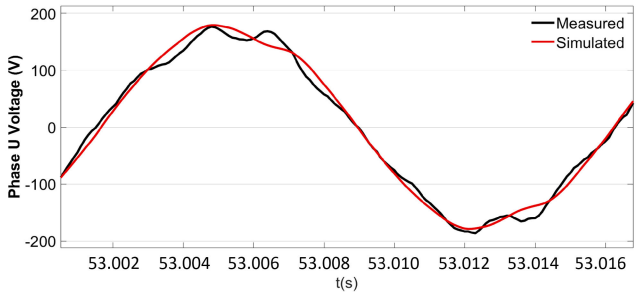

FIGURE 17. Experimental validation under urban drive cycle FTP75 - Phase U Voltage.

The entire two minute drive cycle, simulated with a step size of 0.1 ms, required 6 minutes for execution. In comparison, running a dynamic simulation of this nature within the FEA environment would extend over several days. This is due to the requirement of stepping the rotor by 1 mechanical degree and sampling all signals at a rate of 10 kHz, significantly increasing computational demands and time requirements.

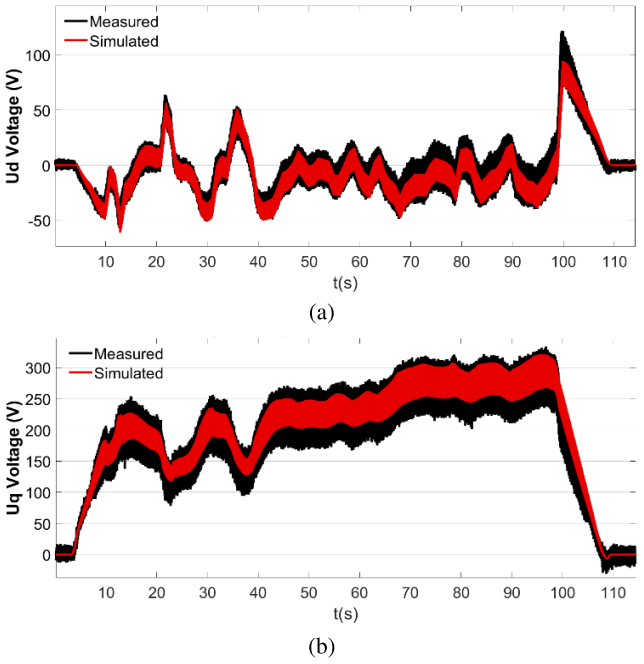

FIGURE 18. Experimental validation under urban drive cycle FTP75. (a) Ud Voltage. (b) Uq Voltage.

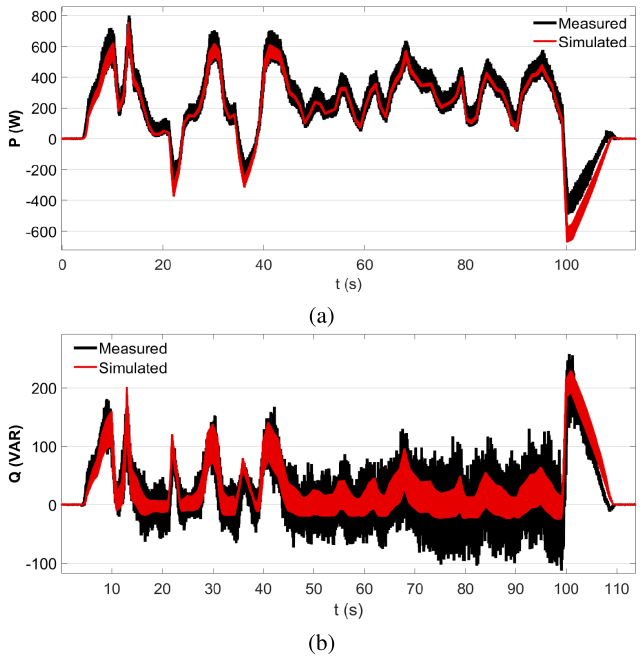

FIGURE 19. Experimental validation under urban drive cycle FTP75. (a) Active Power. (b) Reactive Power.

VI. CONCLUSION

This paper details the construction of a high accuracy hybrid FEA-dq model. The crucial factors in the FEA pre-calculations were identified as the mechanical rotor step size and the current step size. These parameters affect the accuracy of dynamic signals which establishes the total FEA precalculation time for flux linkages and currents. For the PM

machine geometry studied, this amounted to one month of total computation time for the finest resolution dataset.

The main aim of the study was to examine how these step sizes impact the representation of electromagnetic and mechanical signals of the machine. Simulations with the finest step size may not necessarily result in a better accuracy. This was evident in some of the frequency domain signals, where the relative error between measured and simulated values did not decrease with the increase in the resolution of the rotor angle and current. However, the paper has demonstrated a method to balance pre-calculation time against accuracy, for the effective use of hybrid dynamic. This approach may help researchers identify unmodeled effects as the source of discrepancies, rather than attributing them to resolution problems.

Firstly, the study investigated how different mechanical rotor step sizes affect the accuracy and fidelity of the currents and voltages. The simulations indicated that as the rotor step size increased, the harmonic detail reduced, resulting in waveforms with more sinusoidal shape. The selected rotor step size should be less than half the period of the highest harmonic order of interest. In this study, the smallest rotor step size of 1° mechanical, gives up to the 60th harmonic for the stator slot geometry, whilst the largest rotor step size considered could only capture harmonics up to the 2nd order. Selection of a rotor step size to capture expected harmonic indicators is particularly important when assessing harmonic fault signatures. The rotor step angle should not exceed the angular span of one half of the stator slot and stator tooth to capture basic slotting effects.

Furthermore, the effect of current step on the accuracy of machine signals under steady state conditions was examined. No significant differences in magnitude were observed for odd harmonic components. However, the slight winding unbalance in the test machine gives rise to even harmonics, which are over-predicted with the 3 A step compared to the 1 A step, as highlighted in the FFT charts. Entering the overload region of operation could result in a significant difference in signals when employing current steps of different size. Hence, it is essential to understand the saturation characteristics of the machine's materials when choosing a rotor step size. If the region of operation excludes significant saturation, a larger current step size can be used.

Lastly, the simulation models were compared with experiment. The simulated current and voltage waveforms, under nominal speed and a generating load, closely resembled their measured counterparts in the time domain and closely matched the fundamental harmonic in the frequency domain with a discrepancy of below 1%. The difference in magnitude between high order harmonics in current and voltage harmonics can be attributed to a number of factors, such as incomplete knowledge of magnetic materials in the FEA model and assuming that the electrical circuit is balanced by employing the d-q synchronous reference frame in the dynamic simulation. A comparison under dynamic conditions, simulating an urban drive cycle, revealed that the disparity between the measured and simulated values fluctuates, with minimal differences in iq current and Ud and Uq voltage signal amplitudes observed in certain segments of the drive cycle.

In conclusion, it is crucial to set the sampling interval for currents and rotor angle according to the Nyquist sampling theory, although it should be noted that any higher order effects may lead to aliasing. The proposed procedure would run the FEA at no-load, over one electrical rotation, to establish the relationship between flux linkages and angle for the finest rotor step, to identify the frequency of any significant EMF harmonics. Following this, plotting flux linkages against current at 0° and 90° for the finest rotor step can assess the extent of saturation. Step sizes for the desired feature capture can then be selected accordingly.

In this study, the chosen step sizes proved sufficient for accurately capturing the fundamental but lacked the ability to accurately represent many EMF harmonics or slotting effects. The selection of the current step is dependent on the desired level of operation within the saturation region, which is not very significant for the machine under study in this paper.

REFERENCES

[1] Precedence Research. (2022). *Electric Vehicle Market Size, Trends, Growth, Report 2022–2030*. [Online]. Available: https://www.precedenceresearch.com/electric-vehicle-market

[2] (2022). *Decarbonizing Practices in the Global Automotive Industry*. [Online]. Available: https://assets.new.siemens.com/siemens/assets/api/uuid:126d82a4-ff96-4d74-bf52-28281e719488/whitepaper-decarbonizing-practices-in-the-global-automotive-indu.pdf

[3] F. Haces-Fernandez, "Higher wind: Highlighted expansion opportunities to repower wind energy," *Energies*, vol. 14, no. 22, p. 7716, Nov. 2021.

[4] J. Pando-Acedo, A. Rassõlkin, A. Lehikoinen, T. Vaimann, A. Kallaste, E. Romero-Cadaval, and A. Belahcen, "Hybrid FEA-simulink modelling of permanent magnet assisted synchronous reluctance motor with unbalanced magnet flux," in *Proc. IEEE 12th Int. Symp. Diag. Electr. Mach., Power Electron. Drives (SDEMPED)*, Aug. 2019, pp. 174–180.

[5] D. Bobba and B. Sarlioglu, "High fidelity rapid modeling of hybrid rotor PM machines using equivalent machine model," in *Proc. IEEE Transp. Electrific. Conf. Expo (ITEC)*, Jun. 2021, pp. 290–295.

[6] X. Chen, J. Wang, B. Sen, P. Lazari, and T. Sun, "A high-fidelity and computationally efficient model for interior permanent-magnet machines considering the magnetic saturation, spatial harmonics, and iron loss effect," *IEEE Trans. Ind. Electron.*, vol. 62, no. 7, pp. 4044–4055, Jul. 2015.

[7] K. Drobnič, L. Gašparin, and R. Fišer, "Fast and accurate model of interior permanent-magnet machine for dynamic characterization," *Energies*, vol. 12, no. 5, p. 783, Feb. 2019.

[8] B. Sen, J. Wang, and P. Lazari, "A high-fidelity computationally efficient transient model of interior permanent-magnet machine with stator turn fault," *IEEE Trans. Ind. Electron.*, vol. 63, no. 2, pp. 773–783, Feb. 2016.

[9] D. E. Pinto, A.-C. Pop, J. Kempkes, and J. Gyselinck, "dq0-modeling of interior permanent-magnet synchronous machines for high-fidelity model order reduction," in *Proc. Int. Conf. Optim. Electr. Electron. Equip. (OPTIM) Int. Aegean Conf. Electr. Mach. Power Electron. (ACEMP)*, May 2017, pp. 357–363.

[10] H. Elsherbiny, L. Szamel, M. K. Ahmed, and M. A. Elwany, "High accuracy modeling of permanent magnet synchronous motors using finite element analysis," *Mathematics*, vol. 10, no. 20, p. 3880, Oct. 2022.

[11] X. Chen, J. Wang, and A. Griffo, "A high-fidelity and computationally efficient electrothermally coupled model for interior permanent-magnet machines in electric vehicle traction applications," *IEEE Trans. Transport. Electrific.*, vol. 1, no. 4, pp. 336–347, Dec. 2015.

[12] B. Praslicka, C. Ma, and N. Taran, "A computationally efficient high-fidelity multi-physics design optimization of traction motors for drive cycle loss minimization," *IEEE Trans. Ind. Appl.*, vol. 59, no. 2, pp. 1351–1360, Mar. 2023.
[13] A. J. P. Ortega, S. Das, R. Islam, and M. B. Kouhshahi, "High-fidelity analysis with multiphysics simulation for performance evaluation of electric motors used in traction applications," *IEEE Trans. Ind. Appl.*, vol. 59, no. 2, pp. 1273–1282, Mar. 2023.
[14] F. Alvarez-Gonzalez and A. Griffo, "High-fidelity modelling of permanent magnet synchronous motors for real-time hardware-in-the-loop simulation," in *Proc. 8th IET Int. Conf. Power Electron., Mach. Drives (PEMD)*, Apr. 2016, pp. 1–6.
[15] C. Kukura, J. Apsley, and S. Djurović, "Current-to-flux linkage lookup table design for PM machinery FEA-dq hybrid dynamic models," in *Proc. 12th Int. Conf. Power Electron., Mach. Drives (PEMD)*, Oct. 2023, pp. 72–79.
[16] H. Cai and D. Hu, "On PMSM model fidelity and its implementation in simulation," in *Proc. IEEE Energy Convers. Congr. Expo. (ECCE)*, Sep. 2018, pp. 1674–1681.
[17] D. Meeker. (2020). *Finite Element Method Magnetics-Version 4.2 User's Manual*. Accessed: Mar. 25, 2022. [Online]. Available: https://www.femm.info/wiki/Files/files.xml?action=download&file=manual.pd
[18] *Model-Based Calibration Toolbox*. Accessed: Jun. 20, 2022. [Online]. Available: https://uk.mathworks.com/products/model-based-calibration.html
[19] S. Zhu, T. Sun, L. Long, J. Liang, and W. Feng, "A high-fidelity model for FPMSM considering spatial harmonics, mutual inductance, and load change," *Energy Rep.*, vol. 8, pp. 1294–1302, Nov. 2022.
[20] M. B. Marz, "Interharmonics: What they are, where they come from and what they do," in *Proc. Minnesota PowerSyst. Conf. Paper*, 2016, pp. 1–8.
[21] C. Li, W. Xu, and T. Tayjasanant, "Interharmonics: Basic concepts and techniques for their detection and measurement," *Electr. Power Syst. Res.*, vol. 66, no. 1, pp. 39–48, Jul. 2003.
[22] *U.S.: Light-Duty: FTP-75 | Transport Policy*. Accessed: Jan. 15, 2022. [Online]. Available: https://www.transportpolicy.net/standard/us-light-duty-ftp-75/#:~:text=States%20Test%20cycles-
[23] N. Schofield, H. T. Yap, and C. M. Bingham, "Hybrid energy sources for electric and fuel cell vehicle propulsion," in *Proc. IEEE Vehicle Power Propuls. Conf.*, Sep. 2005, pp. 522–529.

CHRISTIAN KUKURA received the M.Eng. degree in electronics and electrical engineering from The University of Glasgow, in 2020. Currently, he is pursuing the Ph.D. degree in electrical engineering with The University of Manchester. His research interests include advanced modeling, condition monitoring, and diagnostics of PMSMs.

JUDITH APSLEY (Senior Member, IEEE) received the B.A. degree in electrical science from the University of Cambridge, in 1986, and the Ph.D. degree from the University of Surrey, in 1996. She is currently a Senior Lecturer in electrical drives, and the Head of the Power Conversion Group, The University of Manchester. Prior to joining The University of Manchester, she worked in industry for 19 years, Westland Helicopters, ERA Technology and LSA Technology. Her research interests include electro-mechanical drive systems. She is CEng and MIET.

SINIŠA DJUROVIĆ (Member, IEEE) received the Dipl.-Ing. degree in electrical engineering from the University of Montenegro, in 2002, and the Ph.D. degree in electrical and electronic engineering from The University of Manchester, in 2007. He is currently a Reader with the Power Conversion Group, The University of Manchester. His research interests include operation, design, monitoring, and diagnostics of electric machines and drives. He serves as an Editor for IEEE TRANSACTIONS ON ENERGY CONVERSION and IEEE ACCESS.